A Bayesian optimization approach to the extraction of intrinsic physical parameters from T_2 relaxation responses

Rupeng Li[1], *Igor* Shikhov[1], and *Christoph H.* Arns[1,*]

[1] UNSW, School of Minerals & Energy Resources Engineering, Sydney 2052 NSW, Australia

Abstract. NMR transverse relaxation responses in porous media provide a sensitive probe of the micro-structure yet are influenced by a set of factors which are not easily detangled. Low-field T_2 transverse relaxation measurements can be carried out quickly and are frequently used to derive pore size distributions and determine derivate parameters like movable fluid volumes or permeability. Here we present an inverse solution workflow extracting related intrinsic physical parameters of the system by tightly fitting experiment and numerical simulation(s). We propose a Bayesian optimization approach that determines five T_2 related properties associated with two values of temperature simultaneously. This concurrent optimization (CO-OPT) utilizes Gaussian process regression to determine the intrinsic physical parameters leading to a match to experiment with a minimal number of function evaluations. A multi-modal search strategy is employed to identify non-unique solution sets of the problem. The workflow is demonstrated on Bentheimer sandstone, identifying five intrinsic physical parameters simultaneously, namely the surface relaxivity of quartz and the effective diffusion and relaxation times of the clay regions at 20° C and 60° C, providing the temperature-dependent quartz surface relaxivity and effective clay parameters. Given the generality of the method, it can easily be adapted to transverse relaxation experiments, or dynamic conditions where e.g., a change in wettability is monitored by intrinsic NMR parameters.

1 Introduction

NMR relaxometry has proven its high value both for laboratory and field petrophysical applications for estimation of pore size distributions [1], saturation of fluids [2], wetting conditions [3] and permeability [4].

The underlying assumption behind – relaxation occurs in fast diffusion regime (a surface governed process) in isolated or weakly coupled pores – must be valid, which is typically the case. This allows representing the observed relaxation rate in saturated rocks $1/T_2$ as a linear sum of three rate processes: bulk fluid relaxation rate $1/T_{2b}$, surface relaxation rate $1/T_{2S}$ and diffusion in the internal field $1/T_{2D}$ [5]

$$\frac{1}{T_2} = \frac{1}{T_{2b}} + \frac{1}{T_{2S}} + \frac{1}{T_{2D}}. \quad (1)$$

Here ρ_2 is transverse surface relaxivity, S and V are surface area and volume of an individual pore. In diamagnetic and weakly paramagnetic rocks, the surface relaxation term, i.e.,

$$\frac{1}{T_{2s}} = \rho_2 \frac{S}{V}, \quad (2)$$

is the primary relaxation mechanism, thus relating the T_2 distribution to pore-sizes. Typically, surface relaxivity is evaluated by matching a T_2 distribution's mode to that of a pore-aperture distribution obtained using mercury intrusion capillary pressure analysis. However, this approach is not entirely problem free, since pore-space geometry and the mode value are practically insensitive to temperature variations in the order of 50° C, while the value of T_2 relaxation distribution mode would noticeably change. It is well known that surface relaxivity is sensitive not only to pore geometry, but also to types of solid and fluid pair, wetting state, and temperature. The latter is also important in the context of calibration of field data with laboratory acquired data. Godefroy et al. [6] developed, and supported experimentally, a theoretical framework describing a surface relaxivity temperature dependency. They established that with increase of the temperature the surface relaxivity of quartz to water in a water-wet sandstone is increasing. Similar observations were reported by [7]. In this work we seek to test further the rarely reported temperature-dependent surface relaxivity behavior in sandstone rocks with the aid of an inverse problem formulation enabling to deduce surface relaxivity and accounting for several temperature effects unaccounted for in the past.

Micro-CT based random walk NMR relaxation simulation allows to easily incorporate effects of faster fluid diffusion at higher temperature, accounts for corresponding change of diffusion governed magnetization exchange, longer bulk water relaxation time etc., as long as corresponding inputs are known (measured). We here exclude from consideration the temperature effect on magnetic susceptibility primarily for the sake of simplicity, but also reasonably assuming

* Corresponding author: c.arns@unsw.edu.au

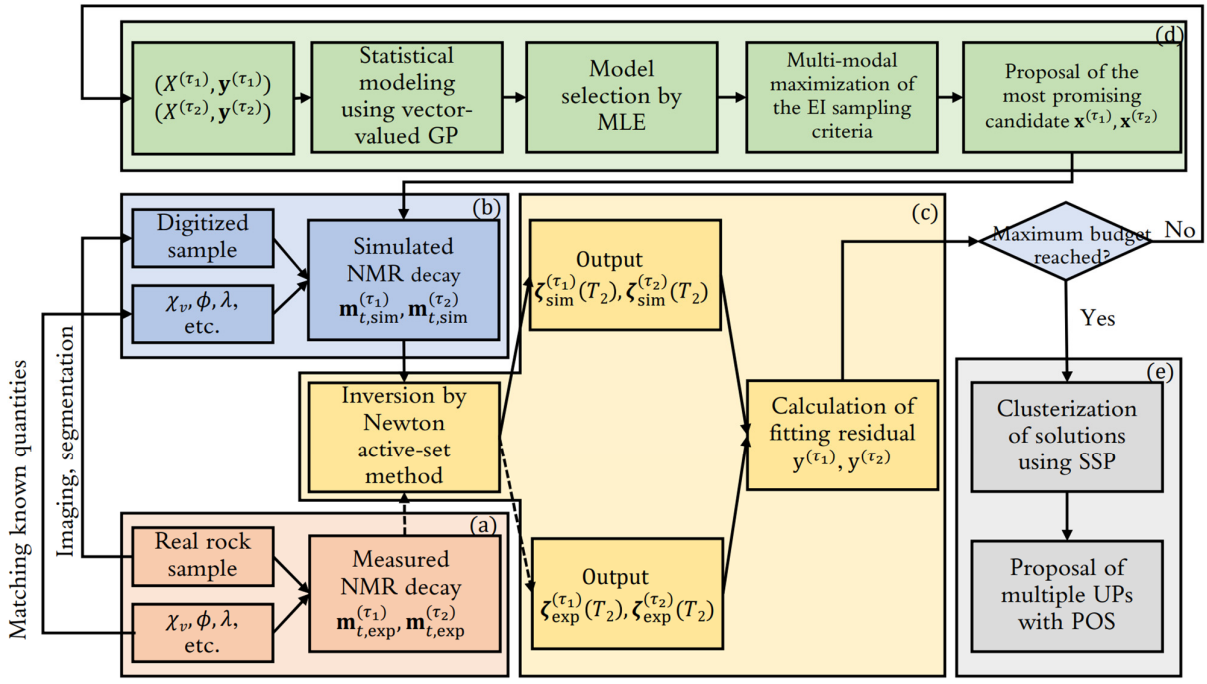

Fig. 1. Flowchart of CO-OPT for the estimation of intrinsic physical parameters from T_2 relaxation responses at two different temperatures.

insignificance of associated effects since the sample rock is diamagnetic, made of mostly of quartz. The magnetic susceptibility of the latter is practically constant in the temperature interval of interest [8]. We note that numerical simulations assign mineral-specific intrinsic properties like surface relaxivity at the pore scale [9-11] while matching distribution modes of experiments results in an effective [12] or apparent surface relaxivity [13; 14].

Given the significant advances in numerical techniques, the temperature-dependent intrinsic parameters can be regarded as unknown and later determined when good matches are achieved between simulations and measurements but is hindered by a practical issue: expensive function evaluations prohibit the enumeration of all configurations of unknown physical parameters in the multi-dimensional solution space. Luckily, the issue of computational burden has been successfully addressed by Bayesian optimization, for which only statistically optimum solutions are proposed for function evaluations, while balancing exploration and exploitation in the solution space. The advantage of Bayesian optimization has been leveraged to recover physical, geometrical, or structural parameters where expensive cost functions are involved [15-17], and in particular, complex multi-physics, multi-parameter, multi-modal problem arising in NMR relaxometry [11]. Furthermore, Bayesian optimization has been integrated with transfer learning for multi-objective optimization, and in particular, for by simultaneous optimization of T_1 and T_2 distributions [18]. In both studies, a multi-modal search strategy, comprising a multi-start L-BFGS-B optimizer searching for local optimum solutions, and a global optimizer social-learning particle swarm optimizer (SL-PSO) for global optimum solutions, are applied to recover all (major) local optimal solutions, i.e., potentially identifying multiple physically valid solution sets.

In this study, we adapt the dual-task inverse solution workflow (DT-ISW) developed for simultaneous fitting of T_1 and T_2 distributions in [18] to the context of simultaneous optimization of T_2 distributions associated with various values of temperature, referred to as concurrent optimization (CO-OPT). We demonstrate the performance of CO-OPT on a Bentheimer sandstone sample by the identification of five intrinsic parameters controlling the NMR relaxation response: one shared quantity, i.e., the tortuosity in clay regions, together with four unique quantities, i.e., transverse surface relaxivity of quartz and effective transverse relaxation time in clay regions, at two values of temperature τ_1 and τ_2. We also provide the SEP as the reference for which the physical quantities related to two values of temperature are separately identified ignoring the constraints that tortuosity is a constant value for a given structure. Finally, we provide the Pareto optimal solutions (POS), which allows operators to balance the preference of T_2 data fits at two values of temperature for the slightly conflicting objectives.

2 Methodology

2.1. Concurrent optimization

As adapted from DT-ISW introduced in [18], CO-OPT is composed of five components: (a) observables, (b) NMR forward solver, (c) cost-function, (d) Bayesian optimization, and (e) solution analysis. Fig. 1 demonstrates CO-OPT using two values of temperature as an example. We briefly summarize these components as itemized list below, while detailed descriptions follow in the next section:

a) Measure the NMR transverse relaxation decays $\mathbf{m}_{t,\mathrm{exp}}^{(\tau_1)}$ and $\mathbf{m}_{t,\mathrm{exp}}^{(\tau_2)}$ at temperatures τ_1 and τ_2.

b) Simulate the decays $\mathbf{m}_{t,\mathrm{sim}}^{(\tau_1)}$ and $\mathbf{m}_{\mathrm{t,sim}}^{(\tau_2)}$ for the chosen sets of unknown intrinsic parameters $\mathbf{x}^{(\tau_1)}$ and $\mathbf{x}^{(\tau_2)}$ on the segmented tomographic images (example: transverse surface relaxivities of the resolved phase: quartz, tortuosity of clay region, effective transverse relaxation times of clay regions), while honoring known quantities like porosity ϕ, volumetric magnetic susceptibility χ_v, bulk physical properties of water, and matching the physical kernel (see Eq. (3)) and regularization parameter λ.

c) Acquire the T_2 distribution using both simulated and measured decays, i.e., $\boldsymbol{\zeta}_{\mathrm{sim}}^{(\tau_1)}(T_2)$ and $\boldsymbol{\zeta}_{\mathrm{exp}}^{(\tau_2)}(T_2)$. Evaluate the cost-function and calculate the sum of the L_2 norm of the fitting residuals for the T_2 distributions.

d) Jointly model the T_2 objective functions at the two values of temperature using the vector-valued Gaussian Process (GP) with correlation captured, followed by inference of model hyperparameters using maximum likelihood estimation; then the EI acquisition function is maximized to identify the promising candidates $\mathbf{x}^{(\tau_1)}$ and $\mathbf{x}^{(\tau_2)}$. Finally, solutions within sparsely explored regions are evaluated using exact simulation.

e) Model the objective functions with the updated model hyperparameters upon depletion of the optimization budget and divide the solution space into various unique partitions (UPs) associated with different modes of the objective function using the solution space partitioning (SSP) introduced in [11]. For each UP the top three solutions and the POS are reported.

2.2 Materials, measurements, and NMR simulations

2.2.1 *Rock Sample*

Experimental reference NMR responses were obtained for a Bentheimer sandstone cylindrical core plug (25 mm diameter and 50 mm long) of 23.9% porosity saturated with 3 wt.% NaCl brine. This rock is composed primarily by quartz (96%) with remaining fraction represented equally by feldspar and kaolinite. The sample has volumetric magnetic susceptibility -7.45 × 10^{-6} (SI units).

2.2.2 T_2 *Reference Data*

We acquire transverse relaxation response of saturated sandstone rock using the standard Carr, Purcell, Meiboom and Gill (CPMG) pulse sequence [19; 20]. The NMR measurements were carried out using a Magritek Rock Core Analyzer operating at 2 MHz proton resonance frequency. Acquired echo-trains were 40,000 echoes long, with echo-time interval 250 us. Summation of 4 scans following phase cycling sequence resulted in a signal-to-noise ratio of around 50. The magnetization decays are treated as multi-exponential sum with unknown distribution of amplitudes $\zeta(T_2)$representing a Fredholm integral equation of the first kind:

$$m_{T_2}(t) = \int_0^\infty \zeta(T_2)\ e^{-t/T_2} \mathrm{d}T_2 + \eta_n(t), \qquad (3)$$

where $m_{T_2}(t)$ is the transverse magnetization decay as function of time t and η_n is additive white noise, and the objective is the estimation of the probability density function of T_2, i.e., $\zeta(T_2)$.

Practically, the T_2 distribution are obtained using a non-negative least squares (NNLS) algorithms, which minimizes the residual sum between the known left-hand size signal and right-hand side prediction, at the same time retaining a degree of control over distribution shape (smoothness) with a penalty/weight term (known as regularization parameter) [21-23]. All experimental and simulated decays were inverted using the algorithm [21] with resulting solutions identically binned across 256 logarithmically spaced T_2 intervals.

2.2.3 *Digitized Image*

A Bentheimer sandstone plug of 5mm diameter was imaged in double helix mode on the UNSW Tyree X-ray CT facility with a total acquisition time of 12h, resulting in a reconstructed tomogram with a resolution of $\epsilon = 2.16$ µm. The grey-scale tomogram was segmented into pore-space, quartz, clay region (a micro-porous effective phase), feldspar and an iron-rich dense mineral phase. For details of the segmentation process see [**Error! Reference source not found.**], which uses the same sample. Fig. 2 depicts a slice through the tomogram and resultant phase segmentation. Statistics of the Bentheimer sandstone segmentations for the calculation of the internal magnetic field at lattice resolution ϵ that follows are listed in Table 1 and Table 2. The micro-CT image was segmented taking into account XRD data reported in [24], though there is a slight difference in between possibly due to mineralogy variation at the mm scale. Basic mineral composition from XRD data and segmented CT image (in brackets) are quartz 96% (96.6%), feldspar 2.4% (1.7%), kaolinite 1.4% (1.6%), others 0.2% (0.15%).

Table 1. Statistics of the Bentheimer sandstone segmentations. Segmented image porosity used in simulation (ϕ_{sim}) is calculated as $f_{\mathrm{p}} + 0.5f_{\mathrm{c}}$ [24], domain size is in voxel, ϵ denotes voxel size, and f_i are phase fractions (f_{p}: resolved porosity, f_{c}: clay region, f_{q}: quartz, f_{f}: feldspar, f_{h}: high-density).

		phase fractions			
ϕ_{sim}	f_{p}	f_{c}	f_{q}	f_{f}	f_{h}
0.2373	0.2252	0.0241	0.7369	0.0126	0.0011

Assuming quartz, feldspar and kaolinite are all iron-free and having similar elemental composition are likely to exhibit similar magnetic susceptibility, susceptibility of bulk sandstone is decomposed into four separate values. Quartz and feldspar are indeed typically reported in a similar range, e.g., Hunt reported -13~-17 × 10^{-6} SI for both [25]. We measured χ_v of fluid and bulk rock only. In particular, χ_v for distilled water and 3% NaCl brine are -8.90 and -9.12 × 10^{-6} SI, respectively, while for convenience we typically use in simulations -9.0 × 10^{-6} SI for aqueous phase [26]. The balance value required to match the average bulk is attributed to a volumetrically small fraction of the high-density minerals assumed to be iron-rich.

Table 2. Measured average volumetric magnetic susceptibilities χ_v, known values for NaCl brine, clay region, quartz, feldspar, and inferred value for high-density using material balance.

volumetric magnetic susceptibilities (SI, multiply by 10^6)					
χ_v	$\chi_{v,w}$	$\chi_{v,c}$	$\chi_{v,q}$	$\chi_{v,f}$	$\chi_{v,h}$
-7.45	-9	$(\chi_{v,w}+\chi_{v,k})/2$	-12	-12	1900

2.2.4 T_2 *Simulation*

Given the naturally discretized segmented tomogram, the NMR responses are simulated via a lattice random walk algorithm following [9-11]. The simulation is carried out in multiple stages: first, the internal magnetic field is calculated in the dipole approximation via a convolution of the susceptibility field as defined by the individual phase susceptibilities given in Table 1 with a dipole field; second, the random walks are carried out on the segmented tomogram with a sub-lattice spacing of $\epsilon/10$ (low temperature) or $\epsilon/15$ (high temperature); random walks are started with a probability linearly related to the porosity of each voxel with each simulation consisting of about 80,000 random walks, dephasing according to the internal fields, with surface interactions lumped into the surface relaxivity for resolved phases, or into a local effective relaxation time for clay regions. Local internal magnetic field values at the required discretization level are derived via tri-linear interpolation from the coarse-scale internal field (resolution of ϵ). Third, the resultant magnetization decay is transformed to the T_2 distribution via an inverse Laplace transform (ILT) [22]. In the optimization framework the phase susceptibilities and the bulk properties of the saturation brine (diffusion coefficient and T_2 bulk relaxation time, see Table 3) are considered as

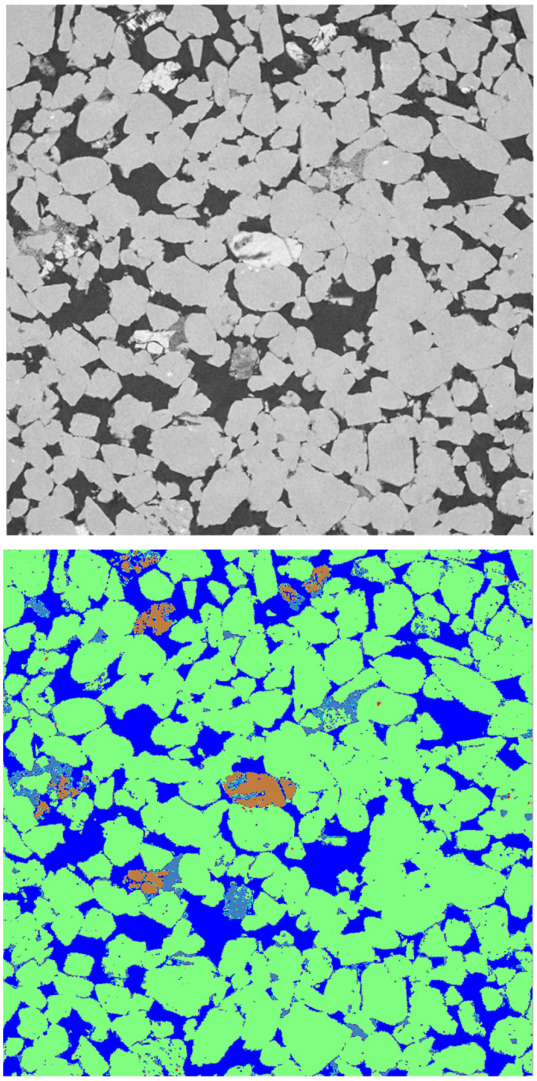

Fig. 2. Slice through the grey-scale tomogram and corresponding five-phase segmentation. Domain size: 1240^3 voxel, voxelsize $\epsilon = 2.16$ µm. Blue: pore, indigo: clay, green: quartz, brown: feldspar, red: high-density phase.

Table 3. Bulk diffusion coefficient and transverse relaxation time of water for the two temperatures considered.

τ / Celsius	$D_0/(\mathrm{cm}^2/\mathrm{s})$	$T_{2b,w}$ / s
20	2.03×10^{-5}	2.27
60	4.76×10^{-5}	5.26

constants. The other pore-scale physical parameters, namely the surface relaxivity of quartz $\rho_{2,q}$, the effective T_2 relaxation time of clay regions ($T_{2e,c}$), and the effective diffusion coefficient of clay regions ($D_{e,c}$) at different temperatures, in the following noted by superscripts (τ_1) and (τ_2), are the target of the proposed optimization effort. The surface relaxivity of minority phases is set to the surface relaxivity of quartz.

2.3 Minimization of T_2 objective under various temperatures

For notational simplicity we describe only two temperatures here, i.e., τ_1 and τ_2. The problem of minimization of the sum of the L2 norm of the fitting residuals for T_2 distributions acquired at τ_1 and τ_2 can be formulated as:

$$\text{minimize} f^{(\text{obj})}(\mathbf{x}) = f^{(\tau_1)}\left(\mathbf{x}^{(\tau_1)}\right) + f^{(\tau_2)}\left(\mathbf{x}^{(\tau_2)}\right), \quad (4)$$

$$\text{where} \quad \mathbf{x} = \left[\mathbf{x}^{(\tau_1)}, \mathbf{x}^{(\tau_2)}\right], \quad (5)$$

$$\mathbf{x}^{(\tau_1)} = \left[\rho_{2,\mathrm{q}}^{(\tau_1)}, T_{2\mathrm{e,c}}^{(\tau_1)}, D_{\mathrm{e,c}}^{(\tau_1)}\right], \quad (6)$$

$$\mathbf{x}^{(\tau_2)} = \left[\rho_{2,\mathrm{q}}^{(\tau_2)}, T_{2\mathrm{e,c}}^{(\tau_2)}, D_{\mathrm{e,c}}^{(\tau_2)}\right], \quad (7)$$

$$\text{subject to} \quad D_{\mathrm{e,c}}^{(\tau_1)}/D_0^{(\tau_1)} = D_{\mathrm{e,c}}^{(\tau_2)}/D_0^{(\tau_2)}, \quad (8)$$

$$\mathbf{x}_\mathrm{l} \le \mathbf{x} \le \mathbf{x}_\mathrm{u}. \quad (9)$$

where $\mathbf{x}_\mathrm{l}$ and $\mathbf{x}_\mathrm{u}$ are the lower and upper bounds of the pre-specified search domain and $f^{(\tau_1)}$ and $f^{(\tau_2)}$ are L2 norm of the fitting residuals for T_2 distributions acquired at temperatures τ_1 and τ_2, respectively, expressed as

$$f^{(\tau_1)}\left(\mathbf{x}^{(\tau_1)}\right) = ||\boldsymbol{\zeta}_{\mathrm{sim}}^{(\tau_1)}\left(T_2|\mathbf{x}^{(\tau_1)}\right) - \boldsymbol{\zeta}_{\mathrm{exp}}^{(\tau_1)}(T_2)||_2^2, \quad (10)$$

$$f^{(\tau_2)}\left(\mathbf{x}^{(\tau_2)}\right) = ||\boldsymbol{\zeta}_{\mathrm{sim}}^{(\tau_2)}\left(T_2|\mathbf{x}^{(\tau_2)}\right) - \boldsymbol{\zeta}_{\mathrm{exp}}^{(\tau_2)}(T_2)||_2^2, \quad (11)$$

with weights for all data points of the T_2 distribution being equally 1. Each lower-dimension component $\mathbf{x}^{(\tau_i)}, i \in \{1,2\}$ is associated with a specific temperature and therefore Eq. (5) specifies the complete solution. The constraints Eq. (8) apply due to Archie's Law, i.e.,

$$\frac{1}{\mathcal{T}} = \frac{D_e}{D_0}, \tag{12}$$

where $\mathcal{T}$ is the tortuosity. We assume that for a given structure the $\mathcal{T}$ is independent of temperature and Eq. (12) holds under both values of temperature.

2.3.1 *Scalar-Valued Gaussian Processes*

GP is a distribution over functions, and is characterized by its mean function $m(\mathbf{x})$ and covariance function $k(\mathbf{x}, \mathbf{x}')$ as [11; 27]

$$f(\mathbf{x}) \sim \mathcal{GP}\big(m(\mathbf{x}), k(\mathbf{x}, \mathbf{x}')\big), \tag{13}$$

where $x = (x_1, x_2, \dots, x_D)^\top$ is a candidate in $\mathcal{X}$ of dimension D × 1, $f(\mathbf{x})$ is the process evaluated at location x. In GP, the prior distribution over f is expressed as

$$\mathbf{f}\,|X \sim \mathcal{N}\left(\mathbf{m}_0, K_f(X,X)\right), \tag{14}$$

where $\mathcal{N}$ denotes normal distribution, $\mathbf{m}_0 \in \mathcal{R}^{n\times 1}$ denotes the mean vector for observations, $(X, \mathbf{y}) = \{\mathbf{x}_i, \mathrm{y_i}\}_{i=1}^n$ and $(\mathbf{x}^*, y^*)$ denotes observed and predicted candidates respectively, and $K_f(X,X)$ denotes the $n \times n$ covariance matrix for $\mathbf{f}$, with the (p,q) entry expressed by $k(\mathbf{x}_p, \mathbf{x}_q)$. Accommodating the noise using Gaussian likelihood function yields $\mathbf{y}|\mathbf{f} = \mathcal{N}(\mathbf{f}, \sigma_n^2 I)$, and the posterior distribution for a single predicted candidate becomes

$$y^*|\,\mathbf{x}^*, X, \mathbf{y}, \boldsymbol{\theta}_s \sim \mathcal{N}\big(\mu(\mathbf{x}^*), \sigma^2(\mathbf{x}^*)\big), \tag{15}$$

where $\mathcal{N}$ is normal distribution, $\boldsymbol{\theta}_s$ is the model hyperparameters for the scalar-valued GP, and

$$\begin{aligned}\mu(\mathbf{x}^*) &= m_0^* + K_f(\mathbf{x}^*, X)\big[K_f(X,X) + \sigma_n^2 I\big]^{-1}(y \\ &\quad - m_0), \\ \sigma^2(\mathbf{x}^*) &= K_f(\mathbf{x}^*, \mathbf{x}^*) + \sigma_n^2 \\ &\quad - K_f(\mathbf{x}^*, X)\big[K_f(X,X) \\ &\quad + \sigma_n^2 I\big]^{-1} K_f(X, \mathbf{x}^*).\end{aligned} \tag{16}$$

2.3.2 *Vector-Valued Gaussian Processes*

GP with multiple outputs can be represented by the vector-valued GP indicates. $Q = 2$ applied throughout this study, indicating that there are two correlated tasks. The GP kernel in Eq. (13) has to be replaced by a vector-valued GP kernel taking into account the correlation between the Q outputs of $\mathbf{f}$, with $\mathbf{f}$ expressed as [28; 29]

$$\mathbf{f}(\mathbf{x}) \sim \mathcal{GP}\big(\mathbf{m}(\mathbf{x}), \mathbf{K}(\mathbf{x}, \mathbf{x}')\big), \tag{17}$$

where $\mathbf{m}(\mathbf{x}) \in \mathcal{R}^{Q\times 1}$ denotes the stacked mean function $\{\mathbf{m}_q(\mathbf{x})\}_{q=1}^Q$ for each output and K denotes a matrix-valued function whose entries $\big(\mathbf{K}(\mathbf{x}, \mathbf{x}')\big)_{q,q'}$ express the correlation between the input-pairs $\mathbf{x}$ and $\mathbf{x}'$, and between the outputs-pairs $f_q(\mathbf{x})$ and $f_{q'}(\mathbf{x})$. We account for the noisy observations using a Gaussian likelihood, i.e., $\mathbf{y}|\mathbf{f} = \mathcal{N}(\mathbf{f}, \Sigma_n \otimes I)$, where $\Sigma_n = \mathrm{diag}(\sigma_n^2)$ is a $Q \times Q$ diagonal matrix incorporating task-dependent noise levels, and $\sigma_n^2 = \big(\sigma_{n,1}^2, \dots, \sigma_{n,Q}^2\big)^\top$ is a vector of noise variances. Similar with the case of scalar-valued GP, the predicted distribution for a single predicted candidate $\mathbf{x}^*$ is expressed as

$$\mathbf{y}^*|\,\mathbf{x}^*, X, \mathbf{y}, \boldsymbol{\theta}_v \sim \mathcal{N}(\boldsymbol{\mu}_{\mathbf{x}^*}, \Sigma_{\mathbf{x}^*}), \tag{18}$$

where $\mathbf{y}^* = \big[y_1^*, \dots, y_Q^*\big]^\top$ concatenates Q outputs for $\mathbf{x}^*$, $\boldsymbol{\theta}_v$ is a vector of model hyperparameters (v stands for vector-valued GP), and

$$\begin{aligned}\boldsymbol{\mu}_{\mathbf{x}^*} &= \mathbf{m}_0^* + \mathbf{K}_f(\mathbf{x}^*, X)\big[\mathbf{K}_f(X,X) + \Sigma_n \otimes I\big]^{-1}(\mathbf{y} \\ &\quad - \mathbf{m}_0), \\ \Sigma_{\mathbf{x}^*} &= \mathbf{K}_f(\mathbf{x}^*, \mathbf{x}^*) + \Sigma_n \\ &\quad - \mathbf{K}_f(\mathbf{x}^*, X)\big[\mathbf{K}_f(X,X) + \Sigma_n \\ &\quad \otimes I\big]^{-1}\mathbf{K}_f(X, \mathbf{x}^*).\end{aligned} \tag{19}$$

2.3.3 Candidate Proposal and Solution Analysis

We use the standard EI acquisition function, which for the q^{th} task is

$$a_{\mathrm{EI},\tau_q}(\mathbf{x}^*) = \int_{-\infty}^{y_q(\mathbf{x}_q^-)} \big(y_q(\mathbf{x}_q^-) - u\big)p(u)\ \mathrm{d}u, \tag{20}$$

where $\mathbf{x}_q^-$ is the current best observed candidate for the q^{th} objective and $u = y_q^*|X, \mathbf{y}, \mathbf{x}^*, \boldsymbol{\theta}_v$ is the Gaussian distributed variable given by Eq. (18).

A promising candidate is proposed by joint maximization of a_{EI,τ_1} and a_{EI,τ_2} in the form of $\sum_{q=1}^2 a_{\mathrm{EI},\tau_q}$ under equality constraints using sequential quadratic programming (SQP) [30]. The initial guesses are placed randomly in the feasible domain, ensuring that the multi-modal nature of the objective function is captured.

When the optimization budget depletes, the model hyperparameters are updated and the T_2 objectives associated with various values of temperature are jointly modelled using new hyperparameters settings. The solution space of Eq. (4) is then divided into various unique partitions (UPs) corresponding to various modes of the objective function. We referred to the solution with the lowest fitness value in each UP is as the local minimum (LM). For details see [11]. Meanwhile, the two objectives are expected to be slightly conflicting since measurements are corrupted by noise so that there is no solution that simultaneously achieves good matches for each objective. As a result, we provide the POS of the T_2 data fits for the slightly conflicting objectives, which is defined as the set of solutions that is not dominated by any other solutions. Mathematically, $\mathbf{x}_1$ dominates $\mathbf{x}_2$ if $\mathbf{x}_1$ beats or ties $\mathbf{x}_2$ for each of the two objectives, i.e., $f^{(i)}(\mathbf{x}_1) \le f^{(i)}(\mathbf{x}_2)$, $\forall i \in \{1,2\}$, and $f^{(i)}(\mathbf{x}_1) < f^{(i)}(\mathbf{x}_2)$, $\exists i \in \{1,2\}$.

3 Results

In this study, we determined the surface relaxivity of quartz and the effective transverse relaxation time and tortuosity for the clay region at two temperatures: $\tau_1 = 20°\mathrm{C}$ and $\tau_2 = 60°\mathrm{C}$, respectively. We compared the speed of convergence, non-unique solution sets as well as the optimum solutions provided by CO-OPT, where tortuosity is a shared parameter for both temperatures and SEP - tortuosity at each

Table 4. The top three candidates in terms of $f^{(\mathrm{obj})}$ (or $f^{(\tau_1)}$ and $f^{(\tau_2)}$ if $f^{(\mathrm{obj})}$ does not exist) within each UP, identified using the two approaches. UPs are sorted in ascending order of the best identified $f^{(\mathrm{obj})}$ within the UP. T_2 distributions corresponding to the LMs are displayed Fig. 3. Both $log_{10}\mathcal{T}$ and $\mathcal{T}$ are reported for convenience. Numbers in the *R* column indicate the rankings of the solutions out of 200 evaluated candidates in terms of $f^{(\mathrm{obj})}$, whereas numbers in the *Step* column indicate at which step those solutions are proposed.

UP	R	$\rho_{2,\mathrm{q}}^{(\tau_1)}$ (μm/s)	$\rho_{2,\mathrm{q}}^{(\tau_2)}$ (μm/s)	$\log_{10}[T_{2\mathrm{e,c}}^{(\tau_1)}(s)]$	$\log_{10}[T_{2\mathrm{e,c}}^{(\tau_2)}(s)]$	$\log_{10}\mathcal{T}$	$\mathcal{T}$	$f^{(\tau_1)}\times10^{-4}$	$f^{(\tau_2)}\times10^{-4}$	$f^{(\mathrm{obj})}\times10^{-4}$	Step
CO-OPT											
1	1	11.169	9.820	-1.889	-2.304	0.535	3.424	2.52	24.23	26.75	131
	2	11.509	10.132	-1.722	-2.143	0.697	4.980	5.61	28.49	34.10	97
	3	9.744	9.978	-1.811	-1.905	0.901	7.956	10.54	27.12	37.66	141
2	4	12.075	9.398	-1.934	-2.530	0.341	2.194	6.45	32.15	38.61	140
	5	12.058	12.103	-2.445	-2.602	0	1	13.13	27.03	40.16	60
	6	12.042	12.100	-2.449	-2.602	0	1	13.31	27.03	40.34	58
SEP, $\tau_1 = 20$°C											
1	1	10.892	-	-1.923	-	0.625	4.213	2.87	-	-	84
	2	11.008	-	-1.943	-	0.593	3.919	3.44	-	-	74
	3	10.895	-	-1.875	-	0.643	4.393	3.85	-	-	196
2	29	11.915	-	-2.406	-	0	1	9.91	-	-	72
	30	11.949	-	-2.397	-	0	1	9.91	-	-	67
	31	12.005	-	-2.389	-	0	1	9.95	-	-	69
SEP, $\tau_2 = 60$°C											
1	1	-	9.068	-	-2.085	0.783	6.067	-	22.64	-	174
	2	-	10.061	-	-1.916	0.895	7.848	-	23.11	-	142
	3	-	8.741	-	-2.101	0.786	6.112	-	24.75	-	195
2	6	-	12.089	-	-2.601	0	1	-	27.03	-	169
	7	-	12.130	-	-2.594	0	1	-	27.05	-	149
	8	-	12.003	-	-2.606	0	1	-	27.08	-	172

temperature is an independent parameter for optimization. Practically the base-10 logarithm of the effective relaxation time and of the tortuosity are employed since they usually vary across orders of magnitude. The solution space is subject to the following bounds:

$$0 \le \rho_{2,\mathrm{q}}^{(\tau_1)}/(\mu\mathrm{m/s}), \rho_{2,\mathrm{q}}^{(\tau_2)}/(\mu\mathrm{m/s}) \le 24,$$
$$-3 \le \log_{10}\left(T_{2\mathrm{e,c}}^{(\tau_1)}/\mathrm{s}\right), \log_{10}\left(T_{2\mathrm{e,c}}^{(\tau_2)}/\mathrm{s}\right) \le 0,$$
$$0 \le \log_{10}\mathcal{T} \le 1.6.$$

The solution space $\mathcal{X}$ composed by such constraints is so large that a grid search or random search is intractable in consideration for the expensive simulation. The optimization budget is 200 function evaluations.

For both approaches here, the multi-modal nature of the objective functions is well-catered, and the non-unique solution sets are identified using solution space partitioning (SSP), clustering all solutions to different UPs. Table 4 shows identified parameter values of the LMs for the two approaches. LMs with $f^{(\mathrm{obj})}$ above 1×10^{-2} are not listed. The problem of non-unique solution sets is encountered in both methods: UP 2 is identified as a mathematically sound solution set, though it is physically less likely since the inferred value for tortuosity reaches the lower bound of 1. Within the physically valid solution set, UP 1, we observe two trends for the variation of surface relaxivity with temperature: Both CO-OPT and SEP consistently show two different response patterns to increase of temperature. Group 1 shows a decrease of surface relaxivity $\rho_{2,\mathrm{q}}$ by about 15%, while group 2 shows a nearly constant surface relaxivity (increase of about 1%). Specifically, for CO-OPT there is a noticeable decrease in $\rho_{2,\mathrm{q}}$, as shown by UP 1, e.g., a decrease from 11.6 μm/s to 9.8 μm/s (averaged over three solutions) while there is a light to no increase in $\rho_{2,\mathrm{q}}$, as shown by the UP 2, e.g., an increase from 12.0 μm/s to 12.1 μm/s. SEP shows the same trend, with surface relaxivity decreasing from 10.9 μm/s to 9.3 μm/s, or increasing from 11.3 μm/s to 11.4 μm/s. We note that the solutions are of low fitness value for both objective functions and thus are considered mathematically correct. The trend is similar for SEP for which there is no constraint to keep tortuosity constant with temperature. As a result, the uncertainty in non-unique solution sets cannot be reduced by examining the quality of fit or the fitness value.

Fig. 3 shows the fit corresponding to the LMs in Table 4. From appearance, the fits for the T_2 distribution at $\tau_1 = 20$°C are better than $\tau_2 = 60$° C for both methods, leading to approximately 10 times larger fitness values at higher temperature. We assume that the larger misfit at higher temperature is mainly a function of increasing diffusion coupling emphasizing the effect of small micro-structural

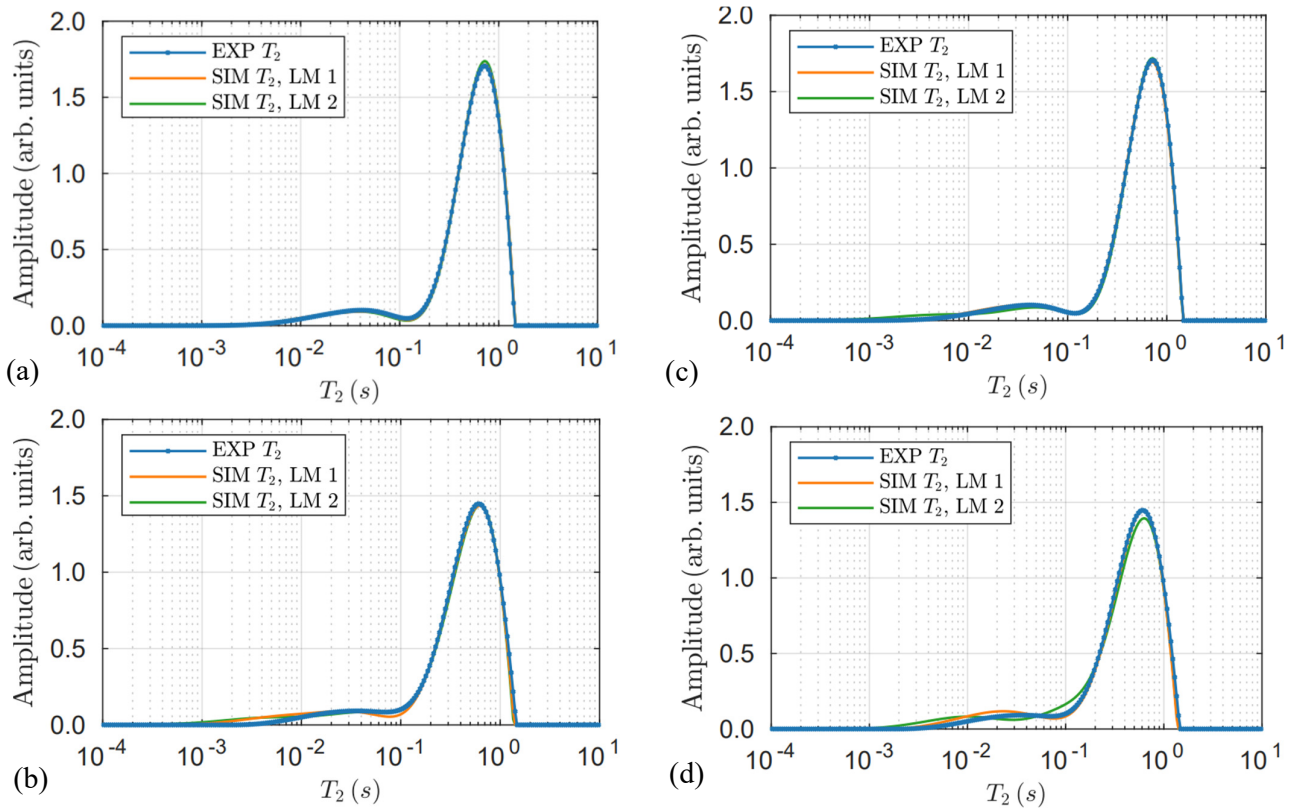

Fig. 3. The T_2 distributions corresponding to the LMs listed in Table 4: (a) CO-OPT, $\tau_1 = 20°C$, (b) CO-OPT, $\tau_2 = 60°C$, (c) SEP, $\tau_1 = 20°C$ and (d) SEP, $\tau_2 = 60°C$.

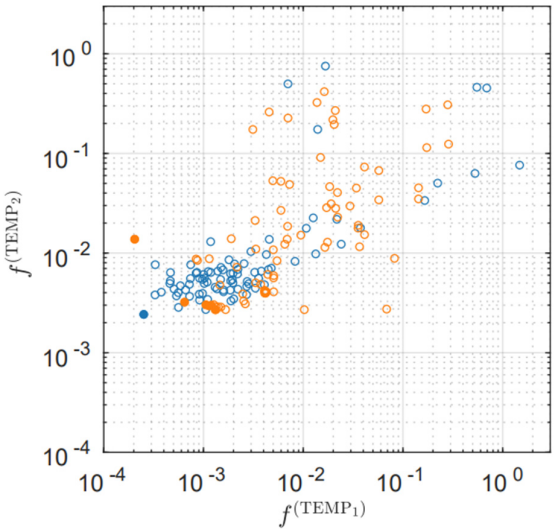

Fig. 4. Minimization of $f^{(\tau_1)}$ and $f^{(\tau_2)}$ using CO-OPT. Candidates in the bottom-left corner are preferred. Solid dots are Pareto optimum solutions; blue and orange dots correspond to UP 1 and UP 2 of CO-OPT in Table 4, and the circles are the dominated solutions.

features in the model.

Here we did not address the mathematical validity for the selection of an optimum solution since the two objectives are slightly conflicting: the $f^{(\tau_1)}$ value of LM 2 is inferior to the second-best solution though it achieves better value for $f^{(\tau_2)}$, as shown in Fig. 4, where candidates in the bottom-left corner are preferred and considered as feasible solutions. Such conflict is also reflected in the result of SEP from Table 4 that if $f^{(\tau_1)}$ and $f^{(\tau_2)}$ are individually optimized, $\mathbf{x}^{(\tau_1)}$ and $\mathbf{x}^{(\tau_2)}$ will neither recover the same value of $\log_{10}\mathcal{T}$ nor satisfy the constraints of Eq. (7). As a result, in situations where the uncertainty in measurement is high, or the conflict between the two objectives cannot be neglected, an optimum solution cannot be solely determined mathematically.

Since it is difficult to visualize the possible solution sets in five-dimensional space, we show in Fig. 5 the isosurface plot of the two objective functions $f^{(\tau_1)}$ and $f^{(\tau_2)}$ for the CO-OPT solution both in the three-dimensional space, as well as the correlation plot between $\rho_{2,\mathrm{q}}$ and $\log_{10} T_{2e,c}$. From both isosurface plots and correlation plots we observe that there are multiple solution sets corresponding to both $f^{(\tau_1)}$ and $f^{(\tau_2)}$, which needs additional physical constraints to reduce such uncertainties.

4 Discussion and Conclusions

In this paper we analyzed the temperature dependent NMR relaxation responses and associated intrinsic physical properties of Bentheimer sandstone, namely the surface relaxivity of quartz and two effective clay parameters, the effective bulk relaxation time $T_{2e,c}$ and the effective diffusion coefficient $D_{e,c}$ of clay, the latter of which was reported as tortuosity to account for its geometric origin and accounting for the expectation that tortuosity remains a constant with respect to temperature. To achieve these aims we introduced

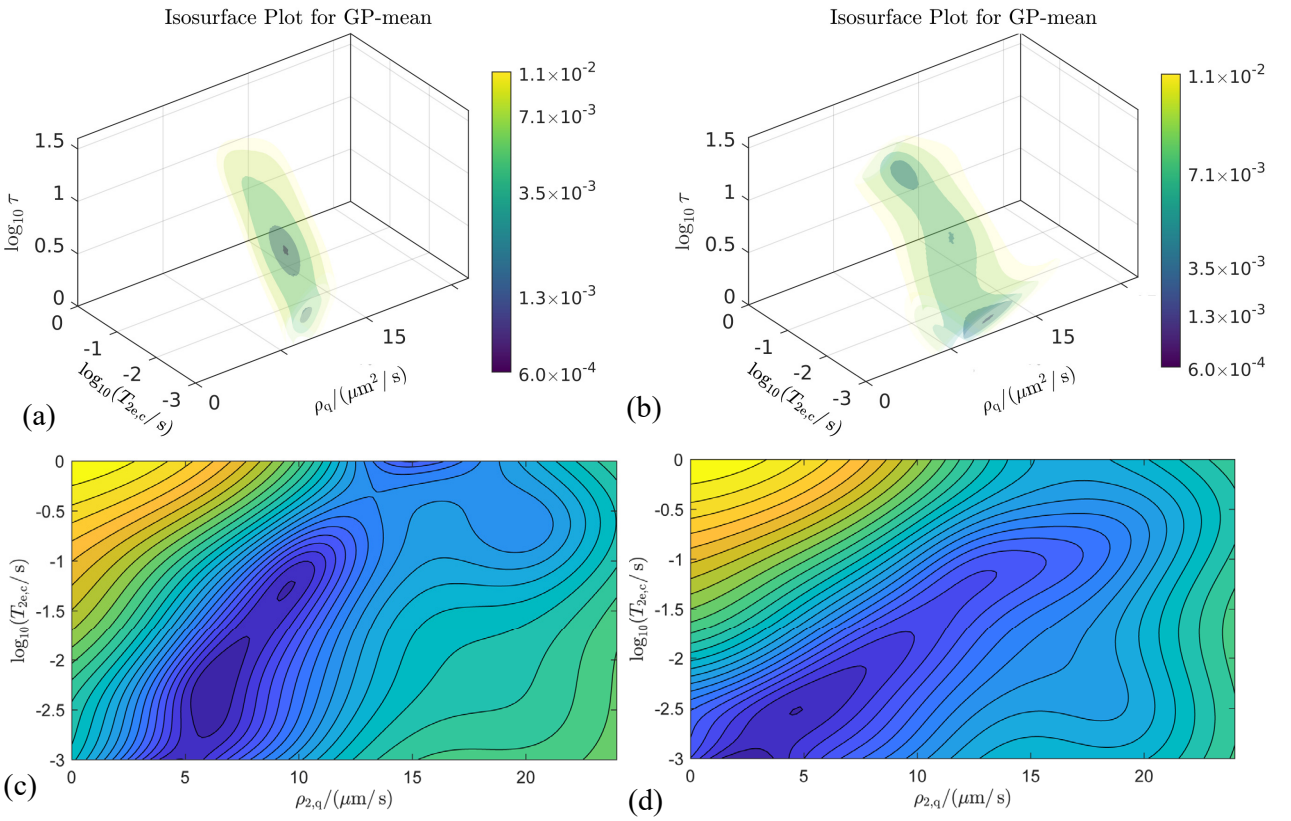

Fig. 5. The isosurface plot of (a) $f^{(\tau_1)}$ and (b) $f^{(\tau_2)}$ each in the three-dimensional space evaluated after the budget of 200 function evaluations is depleted, with contour plots (c) and (d) showing the correlation between $\rho_{2,\mathrm{q}} - \log_{10} T_{2\mathrm{e,c}}$ as projections of the iso-surface plot on to the $\rho_{2,\mathrm{q}} - \log_{10} T_{2\mathrm{e,c}}$ plane. We display five levels of isosurfaces, corresponding to the minimum 0.01%, 0.1%, 1%, 3%, 5% of the scalar field. Blue colors indicate regions with higher probability that mathematically good solutions can be found.

the CO-OPT workflow, which determines the temperature dependent transverse surface relaxivities and effective transverse relaxation time by joint minimization of the deviation between simulated and measured T_2 distributions at two values of temperature: five parameters were identified by computationally producing T_2 distributions almost identical with experiments for two values of temperature.

The experimentally observed enhanced relaxation in Bentheimer sandstone with temperature increase agrees with literature reports. However, contrary to these reports, the mechanisms behind the observed faster relaxation does not require the involvement of a higher surface relaxivity of quartz. We established two solutions, one is that of practically constant surface relaxivity of quartz and another is negatively correlating to temperature (15% lower if temperature is 40 ºC higher). Both solutions enable matching the shift between experimental T_2 distributions, apparently either solely due to faster bulk water diffusion or additionally aided by magnetization coupling between micro- and macro-porosity.

The effective relaxation time of clay decreases by 30-40% with temperature increase. Though we are unable to conclude on specific values since multiple values within a fairly wide interval seem possible (approximately 3 to 15 ms), depending on the analysis method utilized.

The prediction of clay tortuosity is the least certain out of five properties, primarily due to an inherent difficulty of the effective medium approach when applied to dispersed clay in sandstone (in particular for smaller clay pockets/regions). The effect of incorrect magnetization exchange due to unrealistic discontinuity between effective and bulk diffusion at the clay-macropore interface increases with faster diffusion, i.e. is also “temperature-dependent”, and may require a further refinement of numerical simulation.

The results of this study are contrary to what we expected upon starting on this analysis, the target of which was the derivation of the temperature dependence of intrinsic physical properties relevant to NMR relaxation-diffusion responses in rock samples.

We plan to further analyze this behavior in the future with resolved clay [29] and feldspar model structures and increase the resolution of micro-CT images, avoiding the introduction of an effective diffusion coefficient entirely. This should allow us to understand sensitivities and pinpoint the mechanism responsible for the observed behavior. We remark that resolving this issue may have direct implications to the interpretation of NMR responses in the context of wettability alteration, a subject of current intensive study [30].

CHA acknowledges the Australian Research Council for funding through ARC discovery project DP200103548. This work was supported by computational resources provided by the Australian Government through gadi under the National Computational Merit Allocation Scheme (grant m65).

References

1. M. G. Prammer,SPE Annual Technical Conference and Exhibition (1994).
2. W. F. J. Slijkerman, J. P. Hofman, W. J. Looyestijn, Y. Volokitin, Petrophysics - The SPWLA Journal of Formation Evaluation and Reservoir Description, **42**(04) (2001).
3. M. Fleury, F. Deflandre, Magn. Reson. Imaging, **21**(3), 385-387 (2003).
4. A. Timur,SPWLA 9th Annual Logging Symposium (1968).
5. H. C. Torrey, Phys. Rev., **104**(3), 563-565 (1956).
6. S. Godefroy, M. Fleury, F. Deflandre, J. P. Korb, J. Phys. Chem. B, **106**(43), 11183-11190 (2002).
7. K. Katika, H. Fordsmand, I. L. Fabricius, Microporous Mesoporous Mater., **269**, 122-124 (2018).
8. A. Ali, D. K. Potter, Geophysics, **77**(3), WA211-WA221 (2012).
9. C. H. Arns, T. AlGhamdi, J.-Y. Arns, New J. Phys., **13**(1), 015004 (2011).
10. Y. Cui, I. Shikhov, R. Li, S. Liu, C. H. Arns, J. Pet. Sci. Eng., **202**, 108521 (2021).
11. R. Li, I. Shikhov, C. H. Arns, Phys. Rev. Appl., **15**(5), 054003 (2021).
12. J. Chen, G. J. Hirasaki, M. Flaum, J. Pet. Sci. Eng., **52**(1), 161-171 (2006).
13. M. Müller-Petke, R. Dlugosch, J. Lehmann-Horn, M. Ronczka, Geophysics, **80**(3), D195-D206 (2015).
14. S. Costabel, C. Weidner, M. Müller-Petke, G. Houben, Hydrol. Earth Syst. Sci., **22**(3), 1713-1729 (2018).
15. J. Mockus, J. Glob. Optim., **4**(4), 347-365 (1994).
16. D. R. Jones, M. Schonlau, W. J. Welch, J. Glob. Optim., **13**(4), 455-492 (1998).
17. J. Snoek, H. Larochelle, R. P. Adams (2012), in *Proceedings of the 25th International Conference on Neural Information Processing Systems - Volume 2*, edited, pp. 2951–2959, Curran Associates Inc., Lake Tahoe, Nevada.
18. R. Li, I. Shikhov, C. H. Arns, SPE J. (2022).
19. H. Y. Carr, E. M. Purcell, Phys. Rev., **94**(3), 630-638 (1954).
20. S. Meiboom, D. Gill, Rev. Sci. Instrum., **29**(8), 688-691 (1958).
21. C. L. Lawson, R. J. Hanson, Prentice-Hall Inc.
22. P. C. Hansen, Inverse Probl., **8**(6), 849-872 (1992).
23. D. P. Bertsekas, SIAM J. Control Optim., **20**(2), 221-246 (1982).
24. I. Shikhov, D. S. Thomas, C. H. Arns, Energy & Fuels, **33**(9), 8184-8201 (2019).
25. C. P. Hunt, B. M. Moskowitz, S. K. Banerjee (1995), in *Rock Physics & Phase Relations*, edited, pp. 189-204.
26. I. Shikhov, Phd Thesis (2015).
27. C. E. Rasmussen, C. K. I. Williams (2005), The MIT Press.
28. E. V. Bonilla, K. M. A. Chai, C. K. I. Williams (2007), in *Proceedings of the 20th International Conference on Neural Information Processing Systems*, edited, pp. 153–160, Curran Associates Inc., Vancouver, British Columbia, Canada.
29. K. Swersky, J. Snoek, R. P. Adams (2013), in *Proceedings of the 26th International Conference on Neural Information Processing Systems - Volume 2*, edited, pp. 2004–2012, Curran Associates Inc., Lake Tahoe, Nevada.
30. P. T. Boggs, J. W. Tolle, Acta Numer., **4**, 1-51 (1995).